

Effect of Pd ion doping in the band gap of SnO₂ nanoparticles: structural and optical studies

Brajesh Nandan · B. Venugopal ·
S. Amirthapandian · B. K. Panigrahi ·
P. Thangadurai

Received: 4 July 2013 / Accepted: 5 September 2013 / Published online: 21 September 2013
© Springer Science+Business Media Dordrecht 2013

Abstract Pd ion doping has influenced the band gap of SnO₂ nanoparticles. Undoped and Pd ion-doped SnO₂ nanoparticles were synthesized by chemical coprecipitation method. A tetragonal phase of SnO₂ with a grain size range of 7–13 nm was obtained (studied by X-ray diffraction and transmission electron microscopy). A decreasing trend in the particle size with increasing doping concentration was observed. The presence of Pd in doped SnO₂ was confirmed by chemical analysis carried out by energy-dispersive spectroscopy in the transmission electron microscope. Diffuse reflectance spectra showed a blue shift in absorption with increasing palladium concentration. Band gap of SnO₂ nanoparticles was estimated from the diffuse reflectance spectra using Kubelka–Munk function and it was increasing with the increase of Pd ion concentration from 3.73 to 4.21 eV. The variation in band gap is attributed predominantly to the lattice strain and particle size. All the samples showed a broad photoluminescence emission centered at

375 nm when excited at 270 nm. A systematic study on the structural and optical properties of SnO₂ nanoparticles is presented.

Keywords SnO₂ · Nanostructured oxides · Band gap · Electron microscopy · Structural properties · Optical properties

Introduction

Tin oxide (SnO₂) is a n-type wide band gap semiconducting material at room temperature with a band gap of 3.6 eV at 300 K (Robertson 1979). It has a wide range of linear and non-linear applications due to its structural (Wu et al. 1997), optical, and electrical properties in nanoscale dimensions, for example, gas sensors (Shen et al. 2009; Siciliano 2000; Lassesson et al. 2008), solar cells (Sun and Ouyang 2012; Tsai et al. 2011), LEDs (Morgan et al. 2000; Cirpan and Karasz 2006) due to good transparency and conductivity, Li ion batteries (Chandra Bose et al. 2002; Zhang et al. 2011; Zhu et al. 2011) as a anode material, capacitance/supercapacitors (Mu et al. 2011) for rapid transport of the electrolyte ions, electrochemical electrodes (Wang and Wang 2000; Ching et al. 2011), and as a support catalyst material (Marshall and Haverkamp 2012; Shao et al. 2009; Zhang et al. 2010).

With decreasing particle size in nanoscale regime, a drastic change is expected in morphology, structural and optical properties of tin oxide due to a large

B. Nandan · B. Venugopal · P. Thangadurai (✉)
Centre for Nanoscience and Technology, Pondicherry
University, RV Nagar, Kalapet, Pondicherry 605014,
India
e-mail: thangadurai.p@gmail.com;
thangaduraip.nst@pondiuni.edu.in

S. Amirthapandian · B. K. Panigrahi
Ion Beam and Computer Simulation Section, Materials
Science Group, Indira Gandhi Centre for Atomic
Research, Kalpakkam 602105, Tamil Nadu, India

surface to volume ratio and surface-induced defects (Gleiter 1989). There are two major methods which have been used to tune the properties of SnO₂ nanoparticles. The first is the heat treatment at different temperatures. In this method, the particle size may increase with calcinations at higher temperatures. The second one is doping of metal ions. There are many studies reported on tin oxide doped with transition metals (Co, Fe, and Ni) (Siciliano 2000; Ahmed et al. 2011; Sharma et al. 2011); pentavalent elements (Sb) (Marshall and Haverkamp 2012; Shao et al. 2009); and Ti and Zr (Postovalova et al. 2000) for various applications. Li-doped ITO was used to detect the Mn ions (Ching et al. 2011). There is a huge interest in doping catalytic metal ions, Pt and Pd in the SnO₂ host material. These catalytic ions do not affect the structure of the host material but, in fact, improve the gas sensitivity and selectivity, lower the operating temperature, and improve the response time (Shen et al. 2009; Lassesson et al. 2008). Different dopants such as Zn, Ti, or V ions in SnO₂ affect the structure and morphology; and are responsible for smaller crystallite size, creating high surface area and high packing density (Ahmed et al. 2011; Wang et al. 2010). SnO₂ is also used as dilute magnetic semiconductor in spintronics when it is doped with magnetic ions. Recently such oxides having applications in spintronics were found to have room-temperature ferromagnetism (without any dopants) induced by surface oxygen atoms when the particle size is in the range 7–30 nm (Sundaresan et al. 2006). As mentioned before, many studies were reported on the Pd-doped SnO₂ system (Pd:SnO₂) but most of them have focused either directly on the gas-sensing properties or electrical properties (Matko et al. 1999). Reports on band gap tuning by Pd doping in SnO₂ is hardly found and this is the motivation of this work. The objective of the present work is to study the effect of Pd ions on the band gap of SnO₂ nanoparticles and to tune the same. Band gap tuning is successfully reported and supportive results of structural and optical properties were also systematically studied and reported here.

Experimental procedure

Undoped and Pd ion-doped SnO₂ nanoparticles were prepared by chemical co-precipitation method. The advantages of the precipitation methods are the use of

cheap salt precursor, simple operation, and ease of mass production. Moreover, the reaction conditions are mild and adjustable for different purposes (Dhannia et al. 2009). The chemical precursors were 99 % pure tin chloride dihydrate (SnCl₂·2H₂O) (Sigma Aldrich) and 99 % pure palladium chloride (Sigma Aldrich) and they were used as received without any further purification. Aqueous solution of 0.1 M tin chloride dihydrate and PdCl₂ was placed in a beaker and stirred for 1 h at room temperature. Quantity of PdCl₂ was chosen in such a way to give Pd ions concentrations to be 1, 3, and 5 mol% in SnO₂. The homogenized solution was then neutralized by the addition of ammonia solution drop by drop. A white precipitate was formed immediately and that was washed well for a few times with distilled water and dried in air. All the samples were heat-treated at 400 °C for 1 h in air before carrying out all studies.

X-ray diffraction (XRD) patterns were recorded in a powder X-ray diffractometer (STOE diffractometer) by using a Cu-K α ($\lambda = 1.5406 \text{ \AA}$) radiation in Bragg–Brentano geometry in a 2θ range from 0 to 70°. The voltage and current used in the X-ray generator were 40 kV and 30 mA, respectively. Transmission electron microscopy (TEM) studies were carried out in a high-resolution TEM microscope (LIBRA 200FE, Carl Zeiss) at an operating voltage of 200 kV, equipped with EDS (energy-dispersive spectroscopy) detector. It also contains an in-column Ω filter for spectroscopic studies and high-angle annular dark field detector (HAADF). The TEM specimens were prepared by dispersing the SnO₂ nanoparticles in ethanol followed by ultrasonication and a drop of it was laid on a carbon-coated Cu TEM grid. Particle size distribution was obtained from the TEM image analysis. EDS was acquired with 17° tilt of the sample with respect to optic axis and the spectra were collected for 2 min of total collection time.

Fourier transform infrared (FTIR) spectra were recorded using Thermo Nicolet model-6700 spectrometer with a resolution of 0.1 cm⁻¹ on the standard pellet made from SnO₂ with KBr. UV–Vis Spectra were recorded in absorption and diffuse reflectance (DRS) mode in a Varian 5000 UV–Vis spectrometer in the range from 200 to 800 nm with a resolution of 1 nm. Photoluminescence emission spectra were recorded in a fluorescence spectrophotometer (FluoroMax-P, Horiba Jobin Yvon) in the range of 200–500 nm. The emission spectra were recorded

with the excitation wavelength $\lambda_{ex} = 270$ nm. Powder samples were used for UV–Vis and PL spectra acquisition and they were packed in a standard sample holders provided by the company.

Results and discussion

Structure and microstructure studies

Figure 1 presents the XRD patterns of the undoped and Pd:SnO₂ nanoparticles. The diffraction peaks were compared with the standard JCPDS data for SnO₂ (JCPDS file number 41-1445) and they were indexed to the tetragonal rutile phase of SnO₂ and marked in Fig. 1. All the samples were found to be crystalline. The samples are in single phase with no other secondary phases implying a well substitution of Pd ions in SnO₂. Undoped SnO₂ is referred as pure SnO₂ and used as a control sample.

The crystallite size (*t*) was calculated from the FWHM of the 100 % intense diffraction peak of the XRD pattern by using the Debye–Scherrer formula given by

$$t = \frac{0.9\lambda}{\beta \cos\theta} \quad (1)$$

where λ is the wavelength of the X-rays used, β is the full width at half maximum (FWHM), θ is the Bragg angle, and *t* is the average crystallite size. The crystallite size of the undoped SnO₂ is 11 nm; while on doping of Pd ion to the concentration of 1, 3, and 5 mol%, the particle sizes are 13, 10, and 8 nm, respectively. The crystallite size of 1 mol% Pd:SnO₂ is observed to be increased to 13 nm as compared to the same of the pure SnO₂ (11 nm). Perhaps, the following hypothesis is expected to occur during the chemical synthesis for the crystallite size change with Pd ions doping. It is known that the evolution of microstructure of materials depends mostly on the rate of ions transport during the chemical reaction. The rate is expected to be more for the heavier ions than the lighter one in the given medium. Therefore, the lighter Pd ions could have assisted faster assembly of slightly bigger grains of Pd:SnO₂ compared to pure SnO₂. But further increasing the Pd concentration as in case of 3 and 5 mol%, the reactions still become faster and should lead to the bigger crystallite but, due to scattering of ions that participated in nucleation and

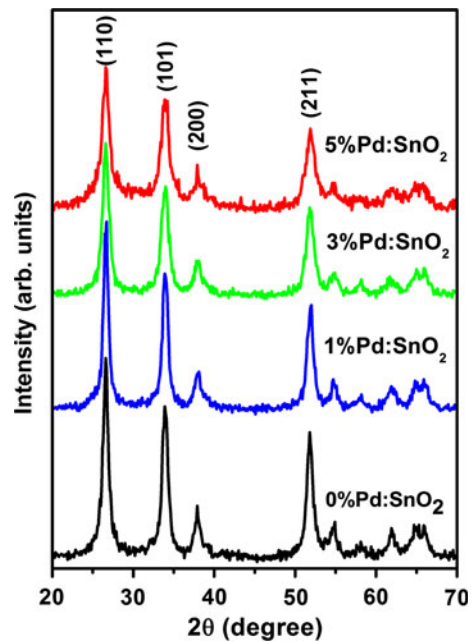


Fig. 1 X-ray powder diffraction patterns of pure and Pd ion-doped SnO₂ nanoparticles (1, 3, and 5 mol% of Pd). Major peaks of tetragonal rutile phase of SnO₂ are indexed

growth, could have caused the smaller crystallite size. There are reports in which particle size was controlled by the synthesis parameters such as concentration of the precursor materials (Ribeiro et al. 2004).

The crystallite size calculation was also done by Williamson–Hall (W–H) (Pal and Chauhan 2007) method. The W–H plot is a plot of $\beta \cos\theta$ versus $4\sin\theta$. Crystallite size can be obtained from the y-intercept whereas the strain value is obtained from the slope of the straight line fit to the data. When the particle size becomes smaller, more lattice strain can be expected in the nanoparticles. This lattice strain will lead to a broadening in the XRD peaks. The width of the diffraction peak depends on particle size, shape, inhomogeneous strain, and instrumentation errors. Strain has a major impact on variation of grain size. Therefore, W–H plot, by taking care of the peak broadening by strain, gives a more accurate particle size estimation. In addition, one can get the strain present in the crystal lattice. The Williamson–Hall formula is given below as,

$$\beta \cos\theta = \frac{k\lambda}{t} + \varepsilon \sin\theta \quad (2)$$

where *t* and ε are the effective particle size and effective strain, respectively, and other symbols hold

the same meaning as in the Scherrer formula. The W–H plot for undoped and Pd:SnO₂ nanoparticles is presented in Fig. 2.

The grain size obtained from the W–H plot for the undoped SnO₂ is 10 nm, and the same for the 1, 3, and 5 mol% Pd:SnO₂ is 11, 9, and 7 nm, respectively. The trend followed by the grain sizes obtained from W–H plot is similar as the crystallite sizes calculated by the Debye–Scherrer formula. The negative slope of the fitted lines in the W–H plot indicates the presence of compressive strain in the lattice of undoped and Pd:SnO₂ nanoparticles. In 1 mol% Pd-doped SnO₂, the compressive strain is less as compared to the pure one. On increasing Pd concentration, the compressive strain increases from -0.01193 to -0.01746 . This behavior of strain with Pd concentration is presented in Fig. 3. The grain size and the strain calculated from the W–H plot are listed in Table 1.

Microstructure of pure and Pd:SnO₂ nanoparticles was studied by TEM microscopy. Typical bright field TEM micrographs of Pd:SnO₂ nanoparticles are presented in Fig. 4. For each sample, low-magnification and high-resolution TEM micrographs are presented along with a selected area diffraction pattern as inset. The shape of the Pd:SnO₂ nanoparticles are nearly spherical in all cases. Particle size distribution in Pd:SnO₂ was estimated from the TEM image analysis by using the ImageJ software. The analysis was carried out on both the bright and dark field images. The histograms of the particle size distribution for the undoped, 1, 3, and 5 mol% Pd:SnO₂ nanoparticles are

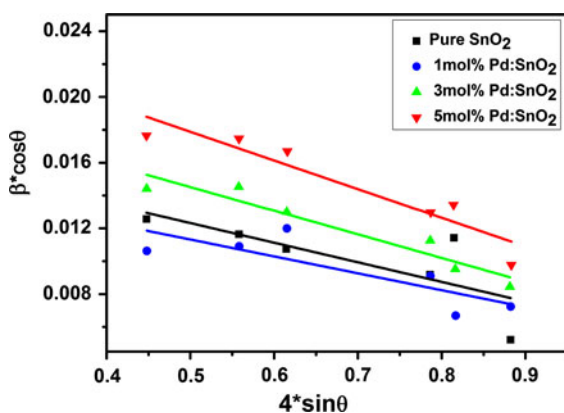


Fig. 2 Williamson–Hall plot for undoped and Pd:SnO₂ nanoparticles. The continuous lines are the straight line fit to the data. Particle size and strain were obtained from the y-intercept and slope of the straight line fit, respectively

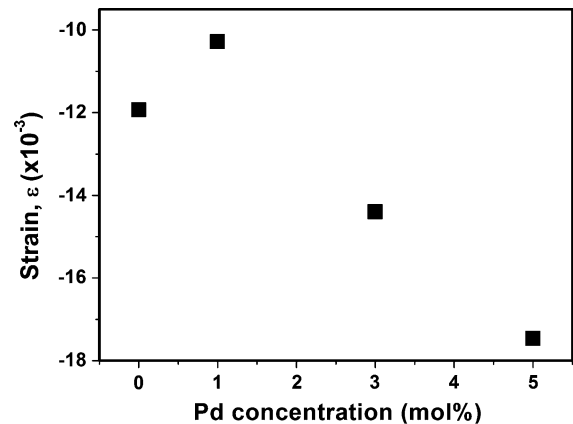


Fig. 3 Variation of strain with doping concentration of Pd ions in Pd:SnO₂ nanoparticles. The strain is compressive in nature

presented in Fig. 5a–d. The histograms were fitted to the log-normal distribution function and the peak values were taken as average particle size that is ranging from 8.8 to 13.1 nm. As we obtained earlier from the XRD analysis, the particle size of the 1 mol% Pd:SnO₂ is slightly higher than the pure SnO₂ and then decreases with further increase of doping concentration. A comparison was made between the particle sizes (see Table 1) calculated from the Debye–Scherrer’s formula, W–H plot, and TEM, and in all cases, they agreed well with each other.

Typical high-resolution TEM images for the Pd:SnO₂ nanoparticles are presented in Fig. 4b, d, f, and h. Inter-planar distance of 0.33 and 0.23 nm have been calculated from the lattice fringes obtained in the HRTEM images and they correspond to (110) and (111) planes, respectively, of the tetragonal phase of SnO₂. The inset of the HRTEM image shows the selected area electron diffraction (SAED) patterns that were indexed to the tetragonal SnO₂. Elemental analysis was performed by EDS spectroscopy and the EDS spectra of Pd:SnO₂ are presented in Fig. 6. The presence of Sn, O, and Pd was studied. The EDS peak at 2.838 eV is present only in the Pd ion-doped samples and absent in the undoped SnO₂. Thus EDS results confirm the presence of Pd in the Pd-doped SnO₂ nanoparticles.

FTIR studies

In the nanoscale materials, the surface is highly sensitive and greatly modified easily. In order to

Table 1 Particle sizes obtained from different methods, strain and band gap energy values for the undoped and Pd:SnO₂ nanoparticles

Sample	Grain size (nm)			Strain (ϵ)	Band gap (eV) from UV-Vis
	Debye-Scherrer formula	W-H plot	TEM image analysis		
Pure SnO ₂	11	10	10.5	-0.01193	3.73
1 mol% Pd:SnO ₂	13	11	13.1	-0.01028	4.03
3 mol% Pd:SnO ₂	10	9	9.1	-0.01440	4.12
5 mol% Pd:SnO ₂	8	7	8.8	-0.01746	4.21

understand the effects of surface modification and removal of impurities from the synthesis, FTIR studies were crucial and carried out. The chemical species present in SnO₂ nanoparticles were investigated by infrared spectra. The FTIR spectra of all the Pd:SnO₂ nanoparticles are presented in Fig. 7. There are several bands present in the wavenumber range 4,000–400 cm⁻¹. The band in the range 3,110–3,431 cm⁻¹ and at 1,635 cm⁻¹ were assigned to the vibration of hydroxyl group due to the absorbed/adsorbed water and showing a stretching vibrational mode of O–H group (Gondal et al. 2010). The bands at 2,356; 2,852; and 2,923 cm⁻¹ belong to the stretching vibrations of C–H bonds that could be from the adsorption and interaction of atmospheric carbon dioxide with water (Gnanam and Rajendran 2010; Tan et al. 2011). The band appeared in the region 400–700 cm⁻¹ is assigned to the Sn–O anti-symmetric vibrations. In that region, the peaks at 560 and 670 cm⁻¹ are assigned to Sn–O and Sn–O–Sn vibrations, respectively (Gondal et al. 2010). In all samples, the vibrations associated to C–H and O–H bonds are seen. This implies that the surface is highly active and adsorbed these molecules. Therefore, if any surface modification is to be done on these samples, de-hydrolysis should be done by heating. Changes observed in the shape, width, and positions of FTIR peaks were attributed to the variation in the local defects, grain size and shape of the nanoparticles (Srinivas et al. 2011).

UV-Vis spectroscopy studies

The effect of Pd ions doping on the band gap of SnO₂ nanoparticles was studied by UV-Vis absorption spectroscopy. The UV-Vis diffuse reflection spectra of the pure and Pd ion-doped SnO₂ nanoparticles are presented in Fig. 8 and its inset shows the magnified view of the region marked with dotted square for better

clarity. With Pd ions concentration, the onset of the reflection spectra is blue shifted.

Experimentally, optical absorption coefficient α of a semiconductor close to the band edge can be expressed by the Tauc plot (Pankove 1971) as given in Eq. 3.

$$\alpha = A(h\nu - E_g)^n / h\nu \tag{3}$$

where α is the absorption coefficient, A is a constant, E_g is the absorption band, $h\nu$ is the photon energy, and n depends on the nature of the transition. That is, n can be 1/2, 2, 3/2, and 3 corresponding to the allowed direct, allowed indirect, forbidden direct, and forbidden indirect transitions, respectively. In this case, $n = 1/2$ that is for direct allowed transition. Figure 9 presents the UV-Vis diffuse reflectance spectra of pure and Pd ion-doped SnO₂ nanoparticles. The band gap energies were calculated using Kubelka-Munk (K–M) model (Tandon and Gupta 1970) which at any wavelength is given by,

$$F(R) = (1 - R)^2 / 2R = k/s = Ac/s \tag{4}$$

where $F(R) = \alpha$ is the K–M function and R is the percentage of reflectance. A graph is plotted between $[F(R)*h\nu]^2$ versus $h\nu$ and the x -intercept value yields the band gap energy. Though the Eq. (3) is enough to calculate the band gap energy from the UV-Vis spectra, we have used the K–M plot for this purpose. Since K–M function is better to be used to derive this parameter from the diffused reflectance spectra of the powder sample (Tandon and Gupta 1970). The K–M plot for the Pd:SnO₂ nanoparticles is presented in Fig. 7. The band gap energies were calculated by extrapolating the absorption to zero absorption coefficients which is calculated from the Eq. (3). The band gap energies thus obtained are 3.73, 4.03, 4.12, and 4.21 eV for the 0, 1, 3, and 5 mol% Pd:SnO₂ nanoparticles, respectively. Change in band gap energy with doping concentration is shown in the inset of

Fig. 4 Bright field TEM micrographs of the undoped (a, b), 1 (c, d), 3 (e, f), and 5 mol% (g, h) Pd:SnO₂ nanoparticles. The *inset* of the high-magnification images is the SAED pattern of the respective samples

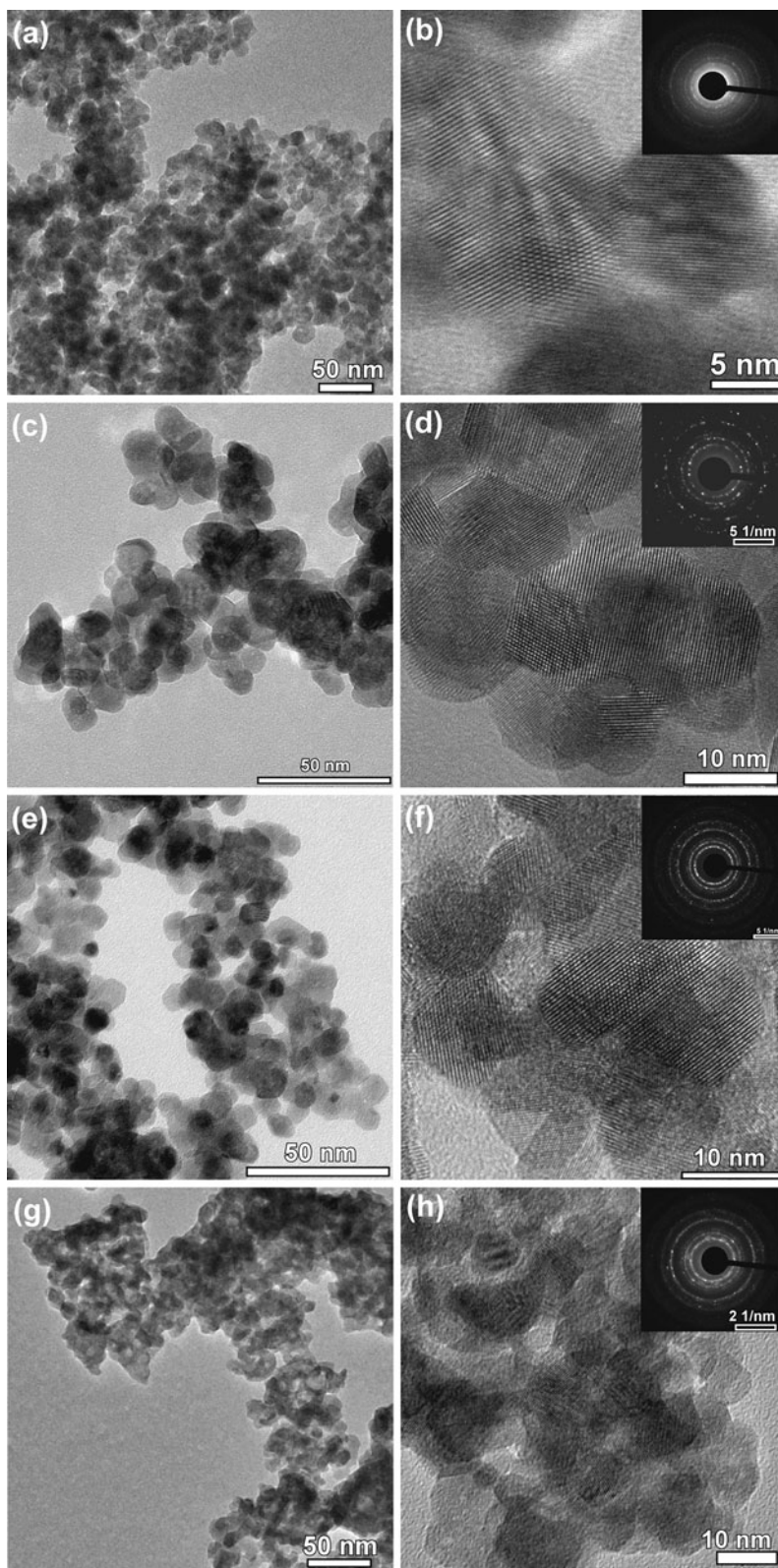


Fig. 5 Particle size distribution of Pd:SnO₂ nanoparticles obtained from the TEM image analysis. The data were fitted to the log-normal distribution. The peak values of the fit were taken as the average particle size of the corresponding samples

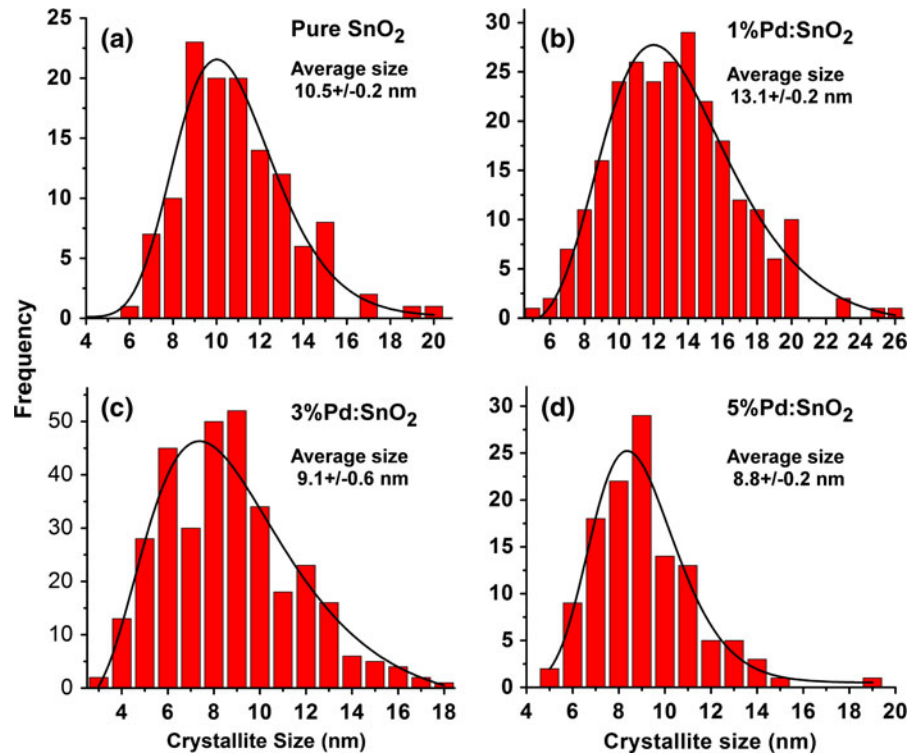


Fig. 9. The band gap energy shows a blue shift with increasing Pd concentration. This increase in band gap with Pd concentration can be attributed either to the decreasing grain size or to strain present in the samples.

Once the increase in E_g is attributed only to the grain size, it is contradicted in the case of 1 mol% Pd:SnO₂; Because, the 1 mol% Pd:SnO₂ sample, by having a higher particle size (than the pure SnO₂), also has the higher band gap energy of 4.03 eV. Therefore, increasing band gap is not only due to the quantum confinement effect, but also due to other factors such as doping concentration (impurity), lattice strain, surface effect, etc. (Smith et al. 2009; Chen et al. 2003), which might be dominated by the later effects. Another reason of increasing band gap energy is the charge transfer transitions between the Pd atom and the SnO₂ conduction or valence band. Similar results have been reported earlier by others researchers (Fang et al. 2008). Generally when the particle radius of the semiconductor is equal or less than excitonic Bohr radius, quantum confinement effect is dominantly observed. When the size of the particle is higher than the excitonic radius, the region is called a weakly confined region and the contribution from the particle

size to the confinement effect will be less. The excitonic Bohr radius of the SnO₂ is 2.7 nm (Ribeiro et al. 2004). In our case, the particle size is greater than the excitonic Bohr radius of SnO₂, which means that they are in the weakly confining region. Hence in our samples, the contribution to be band gap from the particle size is only slight but some other factors are influencing, may be, dominantly. Lattice strain is the next major factor to influence the energy gap of the materials. With further decreasing particle size, more and more compressive lattice strain is expected to be introduced in the lattice. Compressive strain is attributed to the imperfection in the coordination number and also to the bond order loss in nanoparticles (Zhu et al. 2010). This lattice strain is basically due to imperfection or lattice dislocation causing the increment of band gap energy. The lattice strain calculated earlier for pure and Pd:SnO₂ nanoparticles (Table 1) is evident for its presence and contributed to the variation in band gap. The lattice strain was compressive in nature and increasing with the Pd ion concentration. Similar kind of change in band gap was observed in carbon nanotubes and that change was induced by the uniaxial strain (Maki et al. 2007).

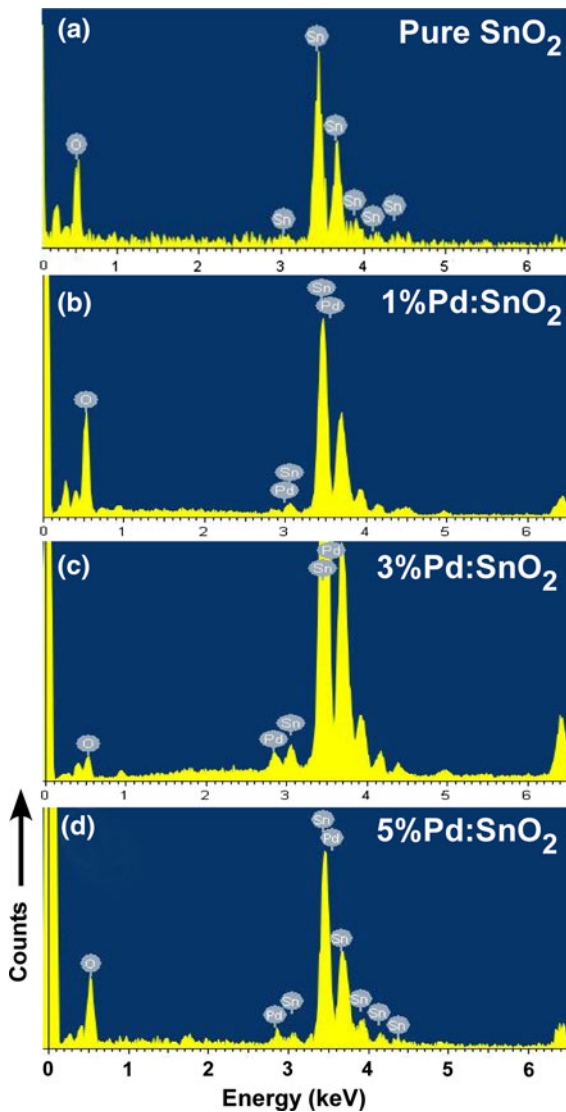


Fig. 6 Energy-dispersive spectra of **a** undoped, **b** 1, **c** 3, and **d** 5 mol% Pd-doped SnO_2 nanoparticles

Photoluminescence studies

Figure 10 shows the PL emission spectra of Pd: SnO_2 nanoparticles acquired at room temperature when excited at 270 nm. All the samples show a strong and broad emission in the ultraviolet region. In literature there were only a few studies made on the Pd ion-doped SnO_2 nanoparticles. It is to be noted that the intensity of the 3 mol% Pd: SnO_2 is lower than the rest of the samples. Intensity is not necessarily to be compared as such because the samples were in powder

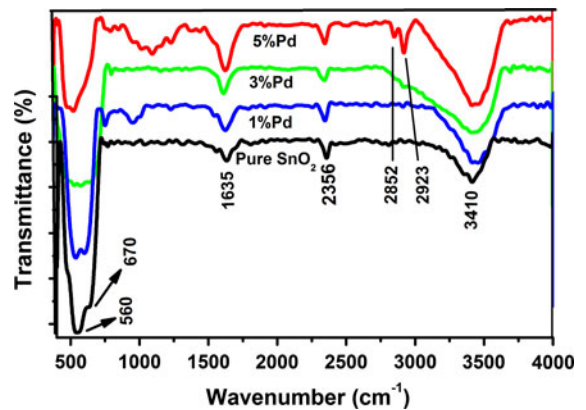


Fig. 7 FTIR spectra of 0, 1, 3, and 5 mol% Pd: SnO_2 nanoparticles. Signatures from the adsorbed O–H and C–H species are also seen

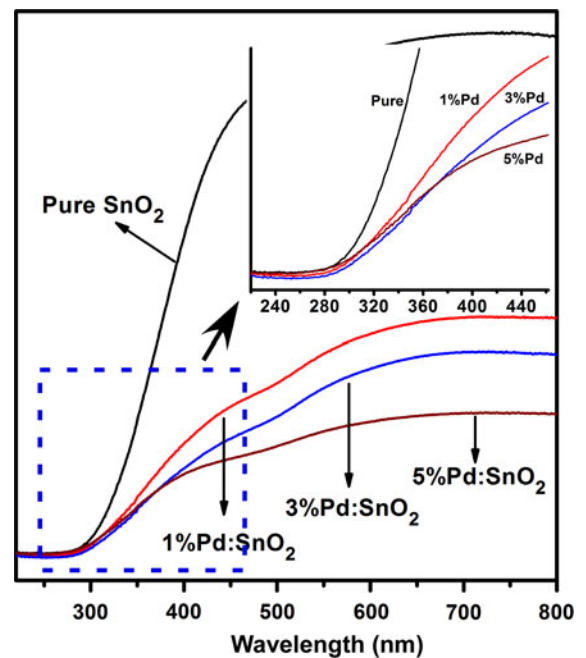


Fig. 8 UV–Vis diffuse reflection spectra of pure and Pd ion-doped SnO_2 nanoparticles. The *inset* is the zoomed spectra of the region marked by *dotted square* for clarity

form and packed manually in the holder and, therefore, only qualitative analysis is to be considered in this case. The emission bands have been observed at 3.69 eV at 250-nm excitation (Pan et al. 2006) for nitrogen-incorporated SnO_2 thin film and 3.16 eV for SnO_2 (Tan et al. 2011) at 275-nm excitation. In the literature, various reports can be found with the emission peaks of SnO_2 that occurred in a range from

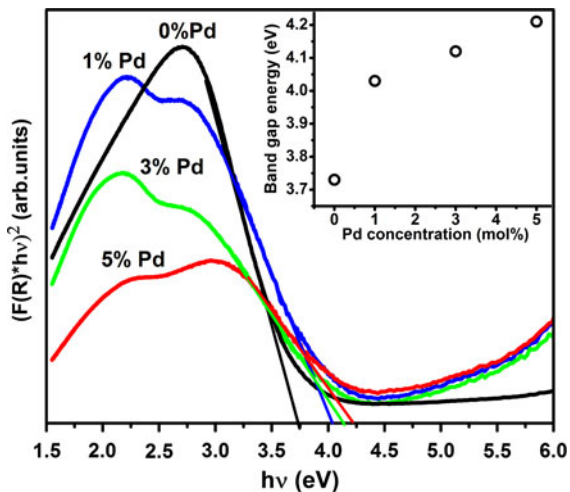


Fig. 9 Diffused reflectance spectra of pure and Pd-doped SnO₂ nanoparticles. The *inset* shows the variation of band gap energy with Pd ion concentration

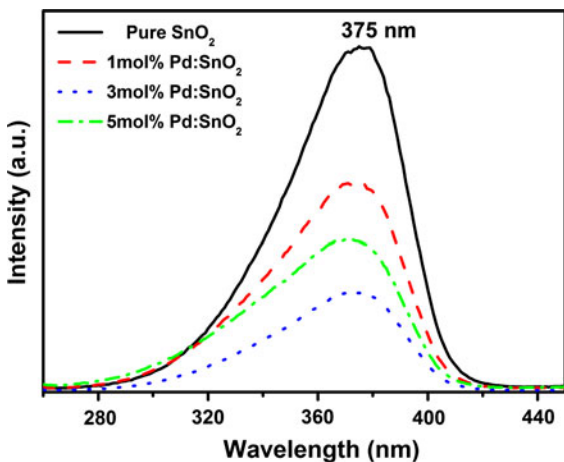


Fig. 10 Photoluminescence emission spectra for pure and Pd ion-doped SnO₂ nanoparticles excited at 270 nm. The emission maximum occurs at 375 nm

318 to 640 nm (Gu et al. 2003; Ahmed et al. 2011; Gondal et al. 2010). Even then the mechanism of PL emission in SnO₂ is not properly understood. In general, one can expect a sharp peak along with a broad spectrum in oxide semiconductors. Generally, two mechanisms of emission in metal oxides are expected. One is a direct recombination of a conduction electron in a Si 4*p* band and a hole in the O 2*p* valence band and usually this gives rise to a sharp emission peak. This is a band edge transition across the band gap of 3.6 eV (for bulk SnO₂). If this is a case,

then the emission corresponding to these transitions should lie in the range 345–350 nm. But, in the present case, the emission peak was observed at 375 nm (3.31 eV). Therefore, the emission through direct recombination across the band gap is not feasible and ruled out. Another mechanism is due to transitions between localized electronic states, which could be due to lattice defects created by impurities, interstitial defects, and dangling bonds (Gu et al. 2003; Hu et al. 2002; Brovelli et al. 2006). This usually gives a broad emission peak assumed to be originated from multiple luminescent centers. It is well known that oxygen vacancies in SnO₂ generate localized states (act as radiative centers in PL) in the form of shallow donor levels approximately 0.03–0.3 eV below the bottom of the SnO₂ conduction band (Brovelli et al. 2006). The considerable number of trap states can also be formed by the Sn vacancies and interstitials. Therefore, the emission related to the transitions with the participation of these shallow levels should be around 375 nm in SnO₂. Based on the discussion above, it is implied that the observed luminescence bands can be correlated to the transitions (shown in Fig. 10) with the participation of shallow acceptor and shallow donor levels.

Conclusions

Nanocrystalline rutile-structured SnO₂ with a size range of 8–13 nm was prepared by a cost-effective preparation method. Grain size obtained by three methods namely Debye–Scherrer formula, W–H plot, and TEM image analysis agree well with each other. FTIR study showed the presence of the adsorbed species implying the importance of heat treatment for high-end applications of these materials. The important feature of this work is the band gap tuning that was achieved by doping Pd ions. The dominant cause for the band gap change is the lattice strain introduced by the doping. Strong PL emission was observed in the UV region. A good optical emitting SnO₂ nanoparticles with band gap tunability was demonstrated in this work.

Acknowledgments The financial supports from the UGC-DAE-CSR (CSR-KN/CRS-14/2011-12/586) and the start-up grant (PU/PC/Start-up Grant/2011-12/311) of Pondicherry University are gratefully acknowledged.

References

- Ahmed AS, Muhamed SM, Singla ML, Tabassum S, Naqvi AH, Azam A (2011) Band gap narrowing and fluorescence properties of nickel doped SnO₂ nanoparticles. *J Lumin* 131:1–6
- Brovelli S, Chiodini N, Meinardi F, Lauria A, Paleari A (2006) Ultraviolet free-exciton light emission in Er-passivated SnO₂ nanocrystals in silica. *Appl Phys Lett* 89:153126
- Chandra Bose A, Kalpana D, Thangadurai P, Ramasamy S (2002) Synthesis and characterization of nanocrystalline SnO₂ and fabrication of lithium cell using nano-SnO₂. *J Power Sources* 107:138–141
- Chen X, Lou Y, Samia AC, Burda C (2003) Coherency strain effects on the optical response of core/shell heteronanostructures. *Nano Lett* 3:799–803
- Ching YM, Tee TW, Zainal Z (2011) Electrochemical studies of Mn(II) mediated by Li⁺ doped indium tin oxide (ITO) electrode. *Int J Electrochem Sci* 6:5305–5313
- Cirpan A, Karasz FE (2006) Indium tin oxide nanoparticles as anode for light-emitting diodes. *J Appl Polym Sci* 99:3125–3129
- Dhannia T, Jayalekshmi S, Santhosh Kumar MC, Prasada Rao T, Chandra Bose A (2009) Effect of aluminium doping and annealing on structural and optical properties of cerium oxide nanocrystals. *J Phys Chem Solids* 70:1443–1447
- Fang LM, Zu XT, Li ZJ, Zhu S, Liu CM, Zhou WL, Wang LM (2008) Synthesis and characteristics of Fe³⁺-doped SnO₂ nanoparticles via sol–gel-calcination or sol–gel-hydrothermal route. *J Alloys Compd* 454:261–267
- Gleiter H (1989) Nanocrystalline materials. *Prog Mater Sci* 33:233–315
- Gnanam S, Rajendran V (2010) Preparation of Cd-doped SnO₂ nanoparticles by sol–gel route and their optical properties. *J Sol–Gel Sci Technol* 56:128–133
- Gondal MA, Drmash QA, Saleh TA (2010) Preparation and characterization of SnO₂ nanoparticles using high power pulsed laser. *Appl Surf Sci* 256:7067–7070
- Gu F, Wang SF, Song CF, Lv MK, Qi YX, Zhou GJ, Xu D, Yuan DR (2003) Synthesis and luminescence properties of SnO₂ nanoparticles. *Chem Phys Lett* 372:451–454
- Hu JQ, Ma XL, Shang NG, Xie ZY, Wong NB, Lee CS, Lee ST (2002) Large-scale rapid oxidation synthesis of SnO₂ nanoribbons. *J Phys Chem B* 106:3823–3826
- Lassesson A, Schulze M, van Lith J, Brown SA (2008) Tin oxide nanocluster hydrogen and ammonia sensors. *Nanotechnology* 19:015502–015508
- Maki H, Sato T, Ishibashi K (2007) Direct observation of the deformation and the band gap change from an individual single-walled carbon nanotube under uniaxial strain. *Nano Lett* 7:890–895
- Marshall AT, Haverkamp RG (2012) Nanoparticles of IrO₂ or Sb–SnO₂ increase the performance of iridium oxide DSA electrodes. *J Mater Sci* 47:1135–1141
- Matko I, Gaidi M, Hazemann JL, Chenevier B, Labeau M (1999) Electrical properties under polluting gas (CO) of Pt- and Pd-doped polycrystalline SnO₂ thin films: analysis of the metal aggregate size effect. *Sens Actuators B* 59:210–215
- Morgan DV, Al-Ofi IM, Aliyu YH (2000) Indium tin oxide spreading layers for AlGaInP visible LEDs. *Semicond Sci Technol* 15:67–72
- Mu J, Chen B, Guo Z, Zhang M, Zhang Z, Shao C, Liu Y (2011) Tin oxide (SnO₂) nanoparticles/electrospun carbon nanofibers (CNFs) heterostructures: controlled fabrication and high capacitive behaviour. *J Colloid Interface Sci* 356:706712
- Pan SS, Ye C, Teng XM, Li L, Li GH (2006) Localized exciton luminescence in nitrogen-incorporated SnO₂ thin films. *Appl Phys Lett* 89(251911):1–3
- Pankove J (1971) Optical processes in semiconductors. Dover Publications, New York
- Postovalova GG, Roginskaya YE, Zav SA, Yalov, BSh Galyamov, Kilmassenko NL (2000) Formation of high conductivity regions in nanostructured SnO₂–AO_x (A = Ti⁴⁺, Zr⁴⁺, Sb³⁺, Sb⁵⁺) films exposed to UV Radiation or H₂. *Inorg Mater* 36:364–374
- Ribeiro C, Lee EJJ, Giraldi TR, Longo E, Varela JA, Leite ER (2004) Study of synthesis variables in the nanocrystal growth behavior of tin oxide processed by controlled hydrolysis. *J Phys Chem B* 108:15612–15617
- Robertson J (1979) Electronic structure of SnO₂, GeO₂, PbO₂, TeO₂ and MgF₂. *J Phys C* 12:4767–4776
- Shao Y, Liu J, Wang Y, Lin Y (2009) Novel catalyst support materials for PEM fuel cells: current status and future prospects. *J Mater Chem* 19:46–59
- Sharma A, Varshney M, Kumar S, Verma KD, Kumar R (2011) Magnetic properties of Fe and Ni doped SnO₂ nanoparticles. *Nanomater Nanotechnol* 1:29–33
- Shen Y, Yamazaki T, Liu Z, Meng D, Kikuta T (2009) Hydrogen sensors made of undoped and Pt-doped SnO₂ nanowires. *J Alloys Compd* 488:L21–L25
- Siciliano P (2000) Preparation, characterisation and applications of thin films for gas sensors prepared by cheap chemical method. *Sens Actuators B* 70:153–164
- Smith AM, Mohs AM, Nie S (2009) Tuning the optical and electronic properties of colloidal nanocrystals by lattice strain. *Nat Nanotechnol* 4:56–63
- Srinivas K, Manjunath Rao S, Venugopal Reddy P (2011) Structural, electronic and magnetic properties of Sn_{0.95}Ni_{0.05}O₂ nanorods. *Nanoscale* 3:642–653
- Sun K, Ouyang J (2012) Polymer solar cells using chlorinated indium tin oxide electrodes with high work function as the anode. *Solar Energy Mater Solar Cells* 96:238–243
- Sundaresan A, Bhargavi R, Rangarajan N, Siddesh U, Rao CNR (2006) Ferromagnetism as a universal feature of nanoparticles of the otherwise nonmagnetic oxides. *Phys Rev B* 74:161306R
- Tan L, Wang L, Wang Y (2011) Hydrothermal synthesis of SnO₂ nanostructures with different morphologies and their optical properties. *J Nanomater*. doi:10.1155/2011/529874
- Tandon SP, Gupta JP (1970) Measurement of forbidden energy gap of semiconductors by diffuse reflectance technique. *Phys Status Solidi* 38:363–367
- Tsai CH, Hsu SY, Huang TW, Tsai YT, Chen YF, Jhang YH, Hsieh L, Wu CC, Chen YS, Chen CW, Li CC (2011) Influences of textures in fluorine-doped tin oxide on characteristics of dye-sensitized solar cells. *Org Electron* 12:2003–2011
- Wang WY, Wang CM (2000) Nanocrystalline tin-oxide modified electrodes and their electrochemical characterization. *J Chin Chem Soc* 47:405–414

- Wang CT, Lai DL, Chen MT (2010) Surface and catalytic properties of doped tin oxide nanoparticles. *Appl Surf Sci* 257:127–131
- Wu X, Zou B, Xu J, Yu B, Tang G, Zhang G, Chen W (1997) Structural characterization and optical properties of nanometer-sized SnO₂ capped by stearic acid. *Nanostructured Mater* 8:179–189
- Zhang P, Huang SY, Popov BN (2010) Mesoporous tin oxide as an oxidation-resistant catalyst support for proton exchange membrane fuel cells. *J Electrochem Soc* 157:B1163–B1172
- Zhang M, Lei D, Du Z, Yin X, Chen L, Li Q, Wang Y, Wang T (2011) Fast synthesis of SnO₂/graphene composites by reducing graphene oxide with stannous ions. *J Mater Chem* 21:1673–1676
- Zhu Z, Ouyang G, Yang G (2010) Bandgap shift in SnO₂ nanostructures induced by lattice strain and coordination imperfection. *J Appl Phys* 108:083511–083514
- Zhu X, Zhu Y, Murali S, Stoller MD, Ruoff RS (2011) Reduced graphene oxide/tin oxide composite as an enhanced anode material for lithium ion batteries prepared by homogenous coprecipitation. *J Power Sources* 196:6473–6477